Phase evolution of vanadium oxides obtained through temperature programmed calcinations of ammonium vanadate in hydrogen atmosphere and their humidity sensing properties

A. A. Akande[1, 2], E. C. Linganiso[1], B. P. Dhonge[1], K. E. Rammutla[2], A. Machatine[3], L. Prinsloo[3], H. Kunert[3], B. W. Mwakikunga[1,*]

[1]DST/CSIR National Centre for Nano-Structured Materials, P O Box 395, Pretoria 0001, South Africa

[2]University of Limpopo, Department of Physics, P/Bag X1106, Sovenga, 0727, RSA

[3]School of Physics, University of Pretoria, Pretoria, 0002, South Africa

Abstract

The possibility of obtaining vanadium dioxide (VO_2) [wherein the vanadium ionic state is 4^+] from a precursor of ammonium metavanadate (NH_4VO_3) bearing the ion V^{5+} is investigated. The reduction is carried out by calcining the NH_4VO_3 powders in similar concentrations of H_2 flow at varying temperatures. The resulting powders have been studied by several techniques including XRD, Raman spectroscopy, FTIR, TEM, BET and DSC. It is found that remnants of bright yellow V^{5+} still exist up to calcination temperatures of 100 ^{0}C after which the sky-blue VO_2 dominates at calcination temperatures of 150 ^{0}C to 250 ^{0}C. There is a population surge of metastable dark-blue V_6O_{13} (where V is in between V^{4+} and V^{5+} ionic states) between 250 ^{0}C and 300 ^{0}C. However above 350 ^{0}C the material reverts to the stable

* Author to whom correspondence is to be addressed:
Bonex Mwakikunga Email address: bmwakikunga@csir.co.za Fax: +27 12 841 2229

V^{5+} in the yellow-orange V_2O_5. XPS/EDS and VSM confirm the order of appearance to be VO_2(150°C) $\rightarrow V_6O_{13}$(200°C)$\rightarrow$ V_2O_5 (350°C).

1. **Introduction**

An oxidation state is influenced by ionization energy while ionization energy depends on the shielding effect between the orbital electron and the nucleus of an atom. In transition metal elements, the electrons enter an inner-shell electron orbital as opposed to other groups where electrons enter the outer-shell electron orbital [1]. The substitution of electrons in the inner-shell in case of transition metals consequently increases the shielding effect, decreases the effective nuclear charge and thereby weakening the ionization energy. All transition metals (Ti, W, Mn, V, Cr, Pd, Pt, Co, Zn, Fe, Cd, Cu, etc.) have low ionization energy, and this makes it less costly to remove more than one electron from their orbitals than it is from compounds with completely filled 3s or 3d orbitals such as alkali metals and alkali earth metal elements. Vanadium is one of these transition metals, it usually presents synthesis difficulties due to its existence in several oxidation states by forming a variety of binary oxides with the following general formulas for n = 1, 2, 3... (1) V_nO_{2n+1} e.g. V_2O_5, V_3O_7, V_4O_9, V_6O_{13}, (2) V_nO_{2n-1} e.g. VO, V_2O_3, and (3) V_nO_{2n} also with VO_2 and V_2O_4 [2]. Among these oxides, V_2O_3, VO_2, V_6O_{13} and V_2O_5 possess many interesting characteristics that can be used in various applications because of their tendency to undergo metal to insulator phase transition commonly known as MIT transition [3-12].

Vanadium dioxide (VO_2) is unique among these oxides because of the abrupt changes in its crystal structure that usually follow the phase transition around 68 ^{0}C. The transition temperature is considerably low and close to room temperature. This MIT property was first observed by F.J. Morin 1959 and later widely studied by Magneli, Mott Hubbard, Peirels,

Goodenough, Adlar, Paquet and Fujimori [3-12]. VO_2 has 4^+ oxidation state oxide of vanadium with a monoclinic (insulating/semiconducting) before transition temperature and tetragonal (metallic) above the transition temperature. Changes in crystal structure explained by Peierls as electron-phonon interaction or coupling, or band structure shift explained by Mott as electron-electron correlation is usually accompanied by a number of physical properties [13]. Such properties are changes in electrical resistance or conductance, optical transmittance or reflectance, phonon frequencies from Raman spectroscopy and FTIR, surface plasmon resonance from absorption spectra and light scattering studies [14, 17-21]. The optical property of VO_2 is also found to be dependent on the surface roughness by AFM studies [15-16]. All these properties make VO_2 feasible for practical application purposes and have been applied in various technological devices. Such devices include smart or switchable window glass panes (thermo-chromic and photo-chromic property) [22-26] as well as gas chemical sensing (gaso-chromic property) [22, 27]. Uses of VO_2 in the fabrication of electrochemical devices (electro-chromic property) have also been recorded [28].

Other oxides such as V_6O_{13} and vanadium pentoxide (V_2O_5) are also relevant as they are close to VO_2 in stoichiometry. V_2O_5 is a V^{5+} oxidation state oxide and is the most stable oxide of vanadium. Its orthorhombic crystal structure usually undergoes metal to insulator phase transition at 375 ^{0}C. V_2O_5 is used as a passive electrode with WO_3 as an active electrode in electro-chromic glass application [28-29]. It has been reported for gas chemical sensing capabilities [30] and also found applications in the lithium ion batteries [31]. V_6O_{13} is known as a mixed valence oxide as it exists between the V^{4+} and V^{5+} oxidation states. [32]. It is monoclinic in crystal structure at both high and low temperature with a characteristic zigzag chain running along the b-axis with mono V^{4+} and mixed V^{4+} and V^{5+} [32]. Its transition temperature is -143 ^{0}C and finds application in lithium ion batteries.

Ammonium meta-vanadate (AMV, NH_4VO_3) has been widely used as a source material for the syntheses of vanadium oxides by various deposition/synthesis techniques, such as chemical precipitation [33, 34], thermal annealing [35], spray pyrolysis [36, 37], and autoclave hydrothermal treatment [38].

In all these synthesis techniques, the phase diagram of V-O system was not followed. As a result, many such reports indicated either single phase VO_2 or V_2O_5 without validation. In this work, we started by thermogravimetry of NH_4VO_3 in nitrogen. Instead of mass loss alone, we also observed mass increase. This prompted further systematic study of phases at various temperatures in hydrogen atmosphere. This paper reports the quantitative study of phases of VO_x at various temperatures. This study sheds more light on the existing phase diagrams of VO_x.

2. **Experimental techniques**

Ammonium metavanadate powder (NH_4VO_3, purity 99.99%, molecular weight of 116. 98 a.m.u, density of 2.3 g $cm^{-1}$and melting (or decomposition) temperature of 200 ^{0}C) was purchased from Sigma-Aldrich Chemical Co. Differential scanning calorimetry (DSC) analysis was performed on the powder using DSC Q2000 V24.4 Build 116 to measure the amount of heat flow into and out of the sample relative to the reference pan with a linear temperature ramp under nitrogen gas. A series of heat treatments were performed for better understanding of the decomposition and phase change in the material. Firstly, heat treatment of the NH_4VO_3 powder was carried out for 400 and 500 ^{0}C in chemical vapour deposition (CVD) reactor under nitrogen flow. This experiment was followed by the TGA measurement of the resulting powder (5.096 mg) and that of standard NH_4VO_3 (4.726 mg) to study the thermal decomposition process in the materials under nitrogen atmosphere. The instrument used is TGA Q500 V20.10 Build 36 by Anton Paar Inc. Further a comprehensive CVD

calcinations of NH_4VO_3 powder under 20 mL min^{-1} hydrogen flow was performed in two different sections, firstly at 100, 150, 200 and secondly at 250, 300, and 350 ^{0}C for 2 hours.

The powder was characterized using an X-Ray diffraction (Panalytical X' pert Pro PW 3040/60 XRD equipped with Cu Kα (λ=0.154*nm*) monochromatic radiation source). XRD patterns were recorded in the scanning range of 5^0-90^0. DSC of these calcined powders was also studied. Raman spectroscopic studies were conducted using a Jobin–Yvon T64000 Raman spectrograph with a 514.5 nm excitation wavelength from an argon ion laser. The power of the laser at the sample was low enough (0.384 mW) in order to minimise localised heating of the sample. The T64000 was operated in a single spectrograph mode, with the 1800 lines/mm grating and a 100x objective on the microscope, and further optical measurements were performed with standard spectrum 100 PerkinElmer FT-IR spectrometer. The microscopic studies and quantitative elemental composition studies were carried out using JEOL 2100 Transmission Electron Microscopy (TEM) (from Tokyo Japan) equipped with LaB6 filament and a Gartan U1000 camera of 2028 X 2028 pixels, and high quality inbuilt Energy dispersive X-ray spectroscopy (EDS).

X-ray photo-electron spectroscopy (XPS) was also performed on a reference sample containing V_2O_5, VO_2, V_6O_{13} as well domains of WO_3. EDS taken from VOx domains (excluding the WO3 domains) in HRTEM was also performed on the same reference sample. The XPS determinations of the proportion of V^{3+}, V^{4+} and V^{5+} were used to calibrate the EDS spectra and this information was then employed in the determination of the proportions of V^{3+}, V^{4+} and V^{5+} for the current set of samples. X-ray photoelectron spectroscopy analyses were carried using a PHI 5000 Versaprobe- Scanning ESCA Microprobe. The survey scans were recorded with a 100 μm, 25 W, 15 kV beam using monochromatic Al K_α radiation (hν = 1486.6 eV) and for the higher resolution spectra the hemispherical analyzer pass energy was maintained at 514 eV to 520 eV (C 1s, O 1s, V 2p) for 50 cycles. Measurements were

performed using either a 1 eV/step and 45 min acquisition time (binding energies ranging from 0 to 1000 eV) for survey scans or a 0.1 eV/step and 20−30 min acquisition times for the high-resolution scans. The pressure during acquisition was typically under 1 × 10−8 Torr. The surfaces were also sputtered clean for 30 s using an Ar ion gun (2 kV energy ions) and measurements were repeated.

The field dependent magnetic characterization was performed using Lakeshore 735 vibrating sample magnetometer (VSM) at room temperature. It is vital to point out that because this type of sample exhibits small magnetization signals, special care was taken during measurements as to avoid any trace magnetic contamination. Magnetic measurements performed on the different batches of VO_x powders showed consistent and reproducible results demonstrating paramagnetic behaviour.

Gas sensing properties were obtained by placing the VO_x paste dispersed in ethanol onto inter-digitated electrodes and obtaining controlled transient readings of current in varying levels of analyte. The measurements were accomplished by employing a Kinosistec (Italy) gas sensor test instrument comprising Keithley voltage and current sources as well as source meters.

3. **Results and Discussions**

3.1 ***Thermal Analysis (DSC/TGA*)**

Fig. 1 (a) shows the DSC profile of NH_4VO_3 recorded in the temperature range of – 47 ^{0}C to 350 ^{0}C and exothermic enthalpy change reaction of about – 38.3 *mW* was observed around 234 ^{0}C which may be due to the decomposition of the material. The other enthalpy change at the 340 ^{0}C is small and may be due to the formation of V_2O_5 phase as it occurred at a temperature close to its phase transition temperature (375 ^{0}C). Fig. 1 (b) shows TGA/DTA profile of NH_4VO_3 recorded in the temperature range of 26 – 900 ^{0}C. The thermogravimetry

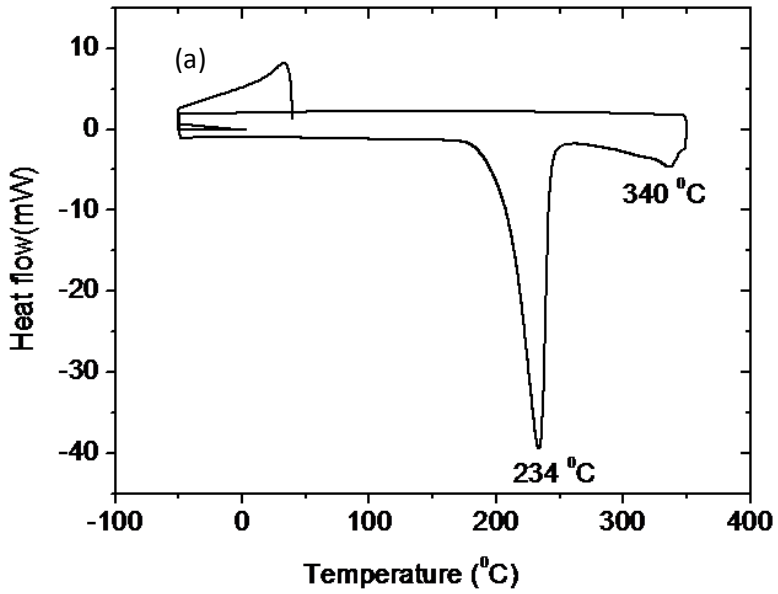

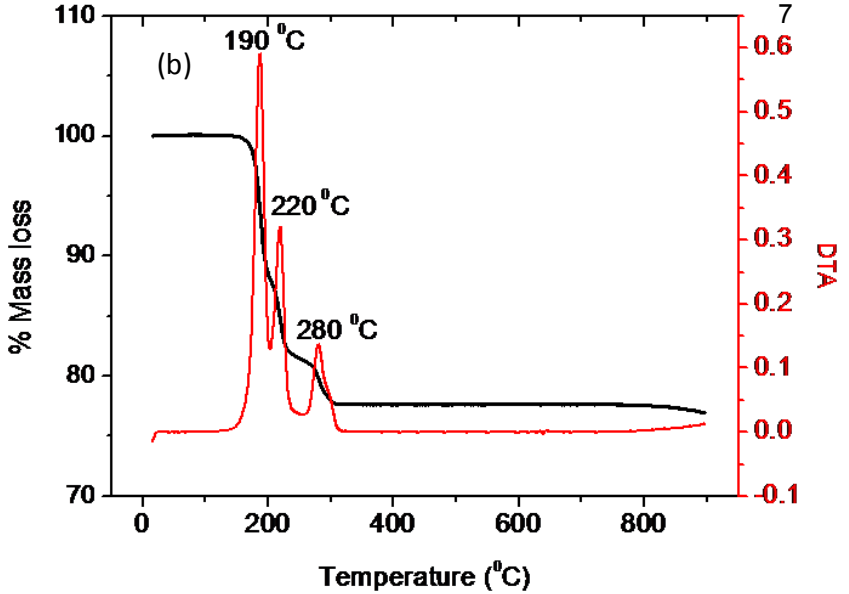

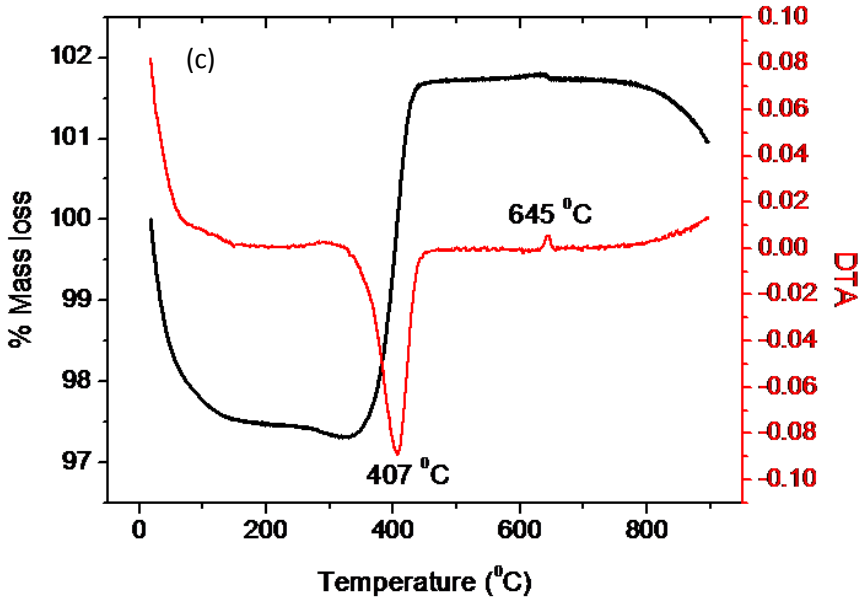

Figure 1 (a): DSC thermogram of the starting precursor (NH4VO3) (b): TGA/DTA thermogram of the starting precursor (NH4VO3) (c): TGA/DTA thermogram of the sample prepared at 400 0C

curve reveals mass loss in three regions during the scan as shown in the figure. The overall mass loss of 22.2% in the material was observed between 155.5 ^{0}C to 309 ^{0}C; this value is in agreement with the one previously reported in the literatures [39-40].

However in this paper we have thoroughly analysed and accounted for each weight loss. Region one lies in the temperature range of 155.4 – 199 ^{0}C, which is accompanied by a mass loss of 11.27%. The mass loss in region twois found to be 6.41% within the temperature range of 199 – 231 ^{0}C and in the third region which falls in the temperature range of 231 – 309 ^{0}C, the loss was found to be 4.52%.

The overall reaction occurs during the decomposition of NH_4VO_3 is shown in Eq. 1, the net mass loss of 22.2 % was observed [40]. The major mass loss occurs due to the evaporation of HN_3 and H_2O.

$$2NH_4VO_3 \rightarrow V_2O_5 + 2NH_3 + H_2O \quad (1)$$

It is believed that the decomposition involve various reaction stages as shown in Eq. 2 to 5 [40-41]. In general, decomposition of NH_4VO_3 initiated according to Eq 2 or 3.

$$6NH_4VO_3 \rightarrow (NH_4)_2V_6O_{16} + 4NH_3 + 2H_2O \quad (2)$$

$$4NH_4VO_3 \rightarrow (NH_4)_2V_4O_{11} + 2NH_3 + H_2O \quad (3)$$

$$3(NH_4)_2V_4O_{11} \rightarrow 2(NH_4)_2V_6O_{16} + 2NH_3 + H_2O \quad (4)$$

$$(NH_4)_2V_6O_{16} \rightarrow 3V_2O_5 + 2NH_3 + H_2O \quad (5)$$

The net mass loss in Eq. 2, 3, 4 and 5 are calculated as 22.2, 11.11, 4.3 and 8.7 % respectively. Representative calculation of mass loss in Eq. 3 is given in the supplementary material SM1 and the same was followed for Eq. 2, 4 and 5. However, the mass loss observed in region one (11.27 %) suggests decomposition of NH_4VO_3 initiated according to Eq. 3.

Thus the further decomposition of out product of Eq. 3 must follow the Eq. 4 and 5. The mass loss in region two (6.41 %) which is higher than the calculated value (Eq. 4). This may due to the simultaneous reactions according to Eq. 4 and 5. This simultaneous reaction is also suggested by the lower observed mass loss (4.52 %) in region three than the calculated (8.7 %) from Eq. 5

Fig. 1(c) is a TGA/DTA profile of the sample prepared at 400 ^{0}C in synthetic nitrogen environment. The scan was performed over the temperature range of 26 – 900 ^{0}C. The XRD profile (attached in SM3) of the powder before TAG measurement reveal the presence of $V_6O_{13.}$ The initial reaction below 100 ^{0}C shows some loss in mass of the powder which may be due to the release of moisture absorbed by the powder. Further increase in temperature up to 335 ^{0}C reveals very small change in mass from 5.096 to 4.972 mg, which is 2.53 %. This is due to the reduction of V_6O_{13}. The possible reduction of V_6O_{13} is shown in Eq. 6. Since the calculated mass loss in Eq. 6 is 3.09 % (attached in SM2) which is very close to observed value.

$$2V_6O_{13} \rightarrow 12VO_2 + O_2 \qquad (6)$$

Above 340 ^{0}C, significant mass gain was observed which was followed by the second stability around 440 ^{0}C. The increase in mass is due to the oxygenation of VO_2. The oxygen is contributed from the synthetic nitrogen flow during TGA experiment. The transformation is ascribed to V_2O_5 since it is known as a most stable oxide among vanadium oxides and usually formed above 340 ^{0}C.

Fig. 2 shows the DSC profiles of the samples prepared by calcination of NH_4VO_3 from 100 - 350 ^{0}C in step of 50 ^{0}C. The peaks at 185 and 220 ^{0}C for the sample calcined at 100 ^{0}C show exothermic reaction which may be due to the release of ammonia. Peaks at 78

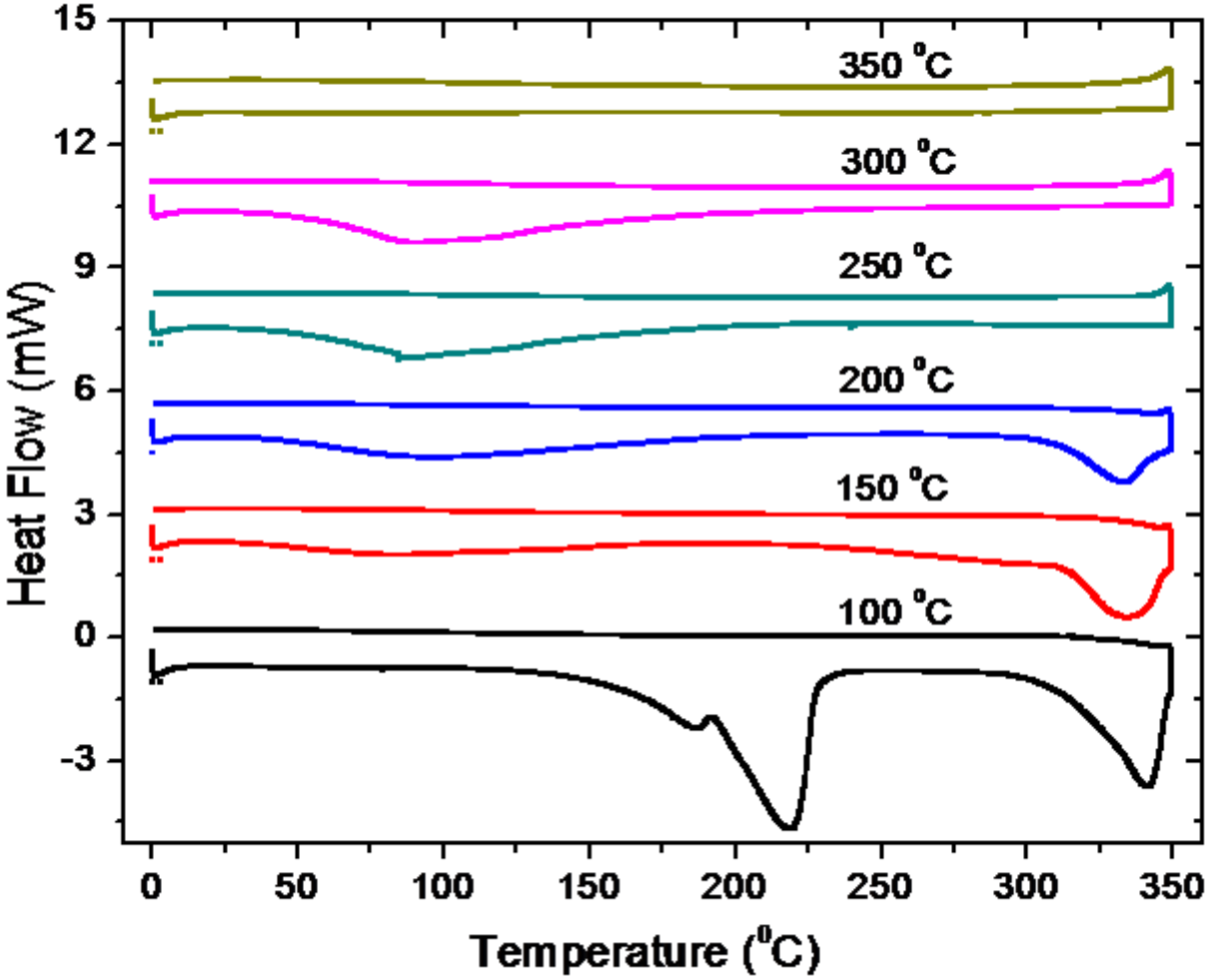

Figure 2: DSC thermograms of the samples prepared by calcination of NH4VO3 from 100 - 350 0C

and 80 ^{0}C for the samples calcined at 150 and 200 ^{0}C may be due to the formation of VO_2, since it is close to MIT temperature and the one at 85 ^{0}C for samples calcined at 250 and 300 ^{0}C may be due to the mixture of metastable phases of VO_2 and V_6O_{13}. The formation of various phase with temperature was confirm with XRD pattern, discussed in section 3.2 and 3.4. The development of V_2O_5 phase was observed for the samples calcined at 100, 150, and 200 ^{0}C in temperature region 310 to 340 ^{0}C. The actual formation of V_2O_5 occurs at 375 ^{0}C. Due to the limitation of DSC in terms of temperature range, we could not proceed for further higher temperature. Although this peak is absent in the case of sample calcined at 250 and 300, this may due to peak shifting to the higher temperature 375 ^{0}C. The sample calcined at 350 ^{0}C show optimum population of phase of V_2O_5,

3.2 ***X-Ray diffraction Spectra***

XRD spectrum of the sample prepared at 400 ^{0}C depicts the monoclinic system of V_6O_{13} by PCPDFWIN CAS No: 72-1278 with (110) plane as the dominant peak. The peaks were rather sharp, which indicate relatively high crystallinity of the particles. The average particle size was determined with Debye-Scherrer's model and found to be around 24 nm. And X-ray diffraction pattern of the sample prepared at 500 ^{0}C also depicts orthorhombic system of V_2O_5 by PCDPDF CAS No: 89-0611 with dominant (101) planes and with presence of plane like (200), (310), (111), (411), (005). The average particle size of 26 nm was observed.

Fig. 3 (a) shows XRD spectra of the standard precursor NH_4VO_3 and samples calcined at temperatures 100 – 350 ^{0}C. The XRD patterns were compared with PCDPDFWIN CAS No: 44-0252, 72-1278 and 89-0611 for VO_2, V_6O_{13} and V_2O_5 respectively. Monoclinic peak of VO_2 at 2θ (diffraction angle) = 27.8 ^{0} corresponding to the plane (011) (PCDPDFWIN CAS No: 44-0252) is found to be dominant among the samples calcined at 100, 150 and 200

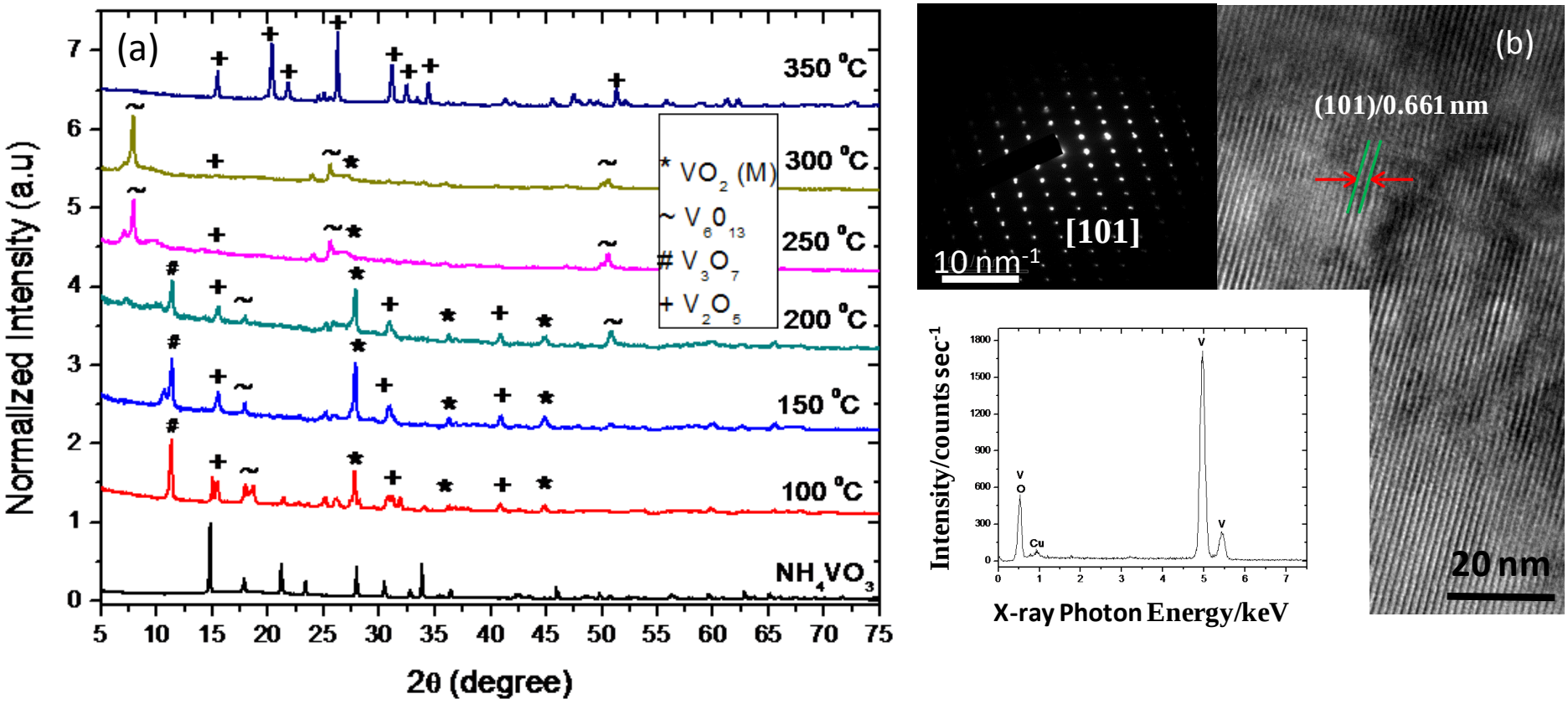

Figure 3 (a): XRD spectra of the standard NH_4VO_3 and of the samples prepared by calcination of NH_4VO_3 from 100 - 350 ^{0}C , (b): High resolution TEM image of sample calcined at 350 ^{0}C showing single plane corresponding to that of 101 of V_2O_5, insert upper corner showing SAED pattern of 101 lattices and insert lower corner showing the corner showing SAED pattern of 101 lattices and insert lower corner showing the corresponding EDS spectrum

^{0}C. Various phases of vanadium oxide were also observed except for those samples calcined at 250 to 350 ^{0}C. The sample prepared at 250 to 350 ^{0}C show the development of single phase of V_2O_5. Predominantly monoclinic metastable V_6O_{13} was observed for the sample calcined at 250 and 300 ^{0}C. Orthorhombic V_2O_5 was observed at 350 ^{0}C.

3.3 *Transmission Electron Microscope*

TEM images for the calcined samples at 150 ^{0}C, 250 ^{0}C and 350 ^{0}C were carried out. fig. 3 (b) shows high resolution TEM image of sample calcined at 350 ^{0}C showing single plane corresponding to that of (101) of V_2O_5. Inset upper corner showing SAED pattern and lower corner showing the corresponding EDS spectrum. Sample calcined at 150 ^{0}C reveals sheet and rod like structure with SAED pattern of non-uniform diffraction. Single (110) plane of uniform diffraction corresponding to that of V_6O_{13} was observed for the sample at 250 ^{0}C. The radius is measured from ImageJ software and the lattice spacing was calculated to be 3.7 Å which is indexed to the monoclinic V_6O_{13} parameters (b=3.671 Å). The calculated value of the lattice spacing for sample calcined at 350 ^{0}C is 3.483 Å which is corresponding to orthorhombic V_2O_5 phase (b=3.517 Å).

3.4 *Phase Diagram*

Fig. 4 is the phase evolution diagram showing the distribution of oxides (VO_2, V_6O_{13} and V_2O_5) with temperature. XRD pattern of sample calcined at various temperatures has been used to developed phase diagram. The phase analysis was carried out by calculating the area of Gaussian fitted XRD peaks. The percentage of phase was calculated using Eq. 7,

$$\%(VO_x) = \frac{\sum A_x}{\sum A_x + \sum A_y + ...} \tag{7}$$

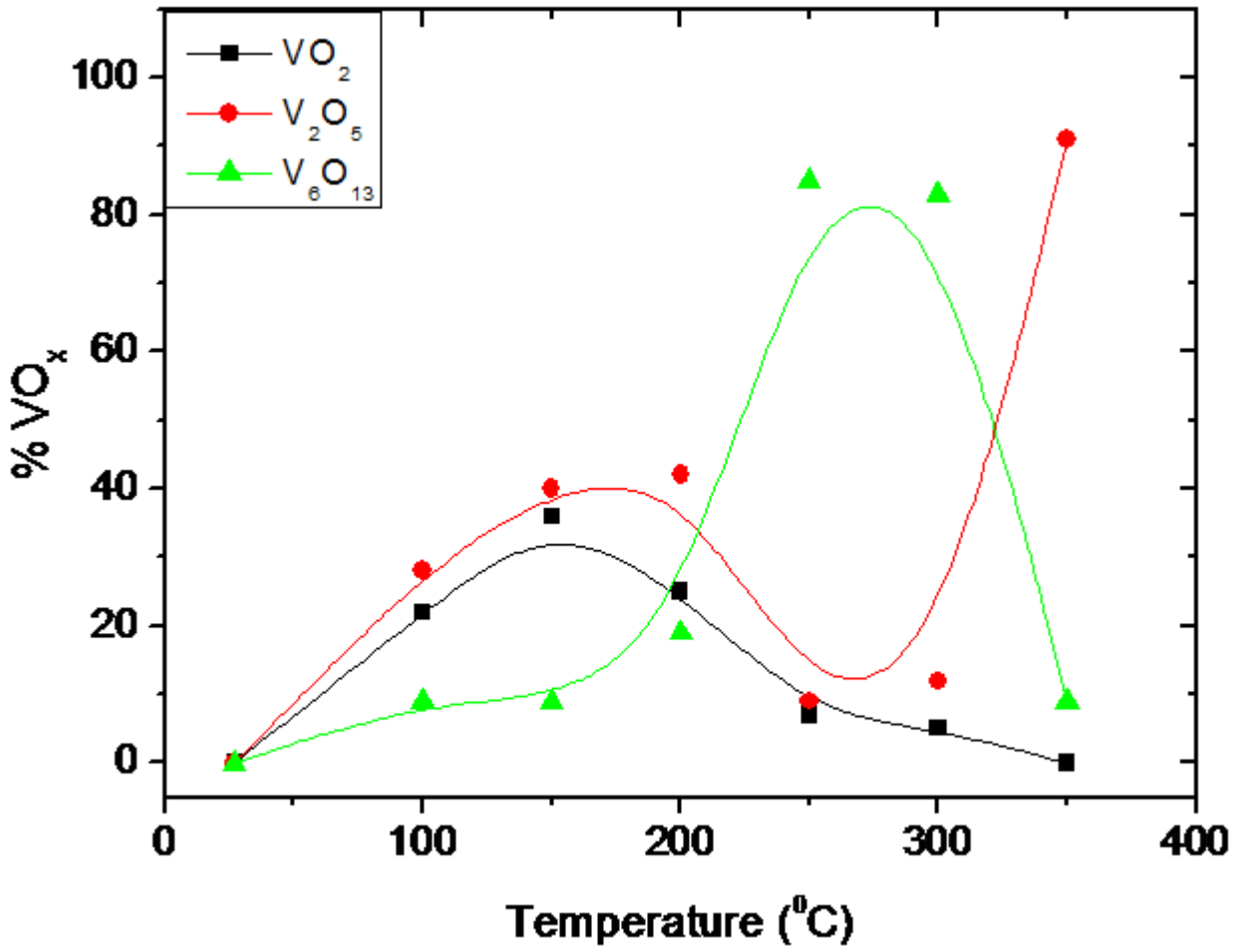

Figure 4: Vanadium Oxides (VO2, V6O13 and V2O5) Phase Evolution Diagram.

where A_x, A_y ….are the peak area corresponding to the phases *x*, *y* ….respectively [47]. It was observed that formation of VO_2 phase dominates in temperature range 150 - 200 ^{0}C, whereas V_6O_{13} phase is the dominant around 250 – 300 ^{0}C. V_2O_5 is found to be present for all temperatures and optimum population at 350 ^{0}C.

3.5 ***Raman Spectroscopy***

Raman spectroscopy is known to be a sensitive and reliable technique for crystal structure study in material science and engineering. This technique is based on the inelastic scattering of monochromatic light irradiated on the sample. The frequency of the scattered light usually collected and compared to that of the incident light. Raman spectrum of the sample prepared at 400 ^{0}C revels all Raman active modes of V_6O_{13} [42]. A strong intense peak at lower frequency band 137 cm^{-1} correspond B_g symmetry and the high frequency vibration at 990 cm^{-1} corresponding to stretching of O-V-O atoms was observed. Vibration modes such as 277, 402 and 523 cm^{-1} are resulting from the bending mode of V-O band and 686 cm^{-1} stretching mode corresponds to the motion parallel and perpendicular to ab-plane [43]. Raman vibrations of the sample prepared at 500 ^{0}C show frequencies 993, 693, 527, 407, 284, 192, 140 cm^{-1} vibrations corresponds modes of V_2O_5 [42-43].

Figure 5 (a) shows Raman spectra of the standard and calcined NH_4VO_3 precursor in the temperature range of 100 - 350 ^{0}C. The presence of 194, 223, 265, 385, 600 and 628 cm^{-1} vibration modes in the samples calcined at 100 – 200 ^{0}C shows the predominant population of VO_2 in this region [42]. The sample calcined at 250 – 350 ^{0}C shows peak at 137, belong to V_6O_{13} phase. The peak at 142 and 992 cm^{-1} belong to V_2O_5 phase [42, 43]. The peaks extra at 265 and 385 cm^{-1} revels the presence of VO_2 phase at higher temperatures. The peak due to ammonia vibrations is observed around 1420 cm^{-1} for precursor NH_4VO_3 [44].

3.6 ***Fourier Transform Infrared Spectroscopy (FT-IR)***

FT-IR is a rotational vibrational spectroscopic technique that is based on the absorption of photon by the molecules constituting a material. Molecule absorbs the incident photon and promote to higher energy state (excited state). The changes in energy of incident photon due to the absorption were detected. Fig.5 (b) shows the FTIR spectra of the standard and calcined NH_4VO_3 precursor in the temperature range of 100 - 350 ^{0}C.

The observed absorption shoulder at 715 cm^{-1} and strong peak at 972 cm^{-1} are correspond to the VO_2 [45], The shoulder at 715cm^{-1} was not observe for higher temperature (250 – 350 ^{0}C) and the shift in 972 cm^{-1} peak was observed at 350 ^{0}C. The peak shifted to higher frequency 1009 cm^{-1} at 350 ^{0}C corresponding to single polycrystalline V_2O_5 phase [45]. The presence of both shoulder and strong peak at lower temperature (100 – 200 ^{0}C) reveals the higher population of VO_2. The higher population of V_2O_5 at higher temperature and VO_2 at lower temperature is also supported by our XRD phase calculation and Raman study.

3.7 ***Brunauer-Emmett-Teller (BET)***

Brunauer-Emmiter-Teller theory relies on the physical adsorption (physisorption) of gas molecules on the surface of solid-state materials. This technique gives information about the specific surface area of a nano-material. This theory is an extension of Langmuir theory which described the amount of adsorbs molecules (adsorbate) on the surface of material (adsorbent) as a function of pressures or concentration [46]. BET equation is expressed below in Eq. (8),

$$\frac{1}{v(\frac{p_0}{p}-1)} = \frac{c-1}{v_m c}(\frac{p}{p_0}) + \frac{1}{v_m c} \qquad (8)$$

where p and p_0 are the equilibrium and saturation pressure of adsorbate at the temperature of adsorption, v is the adsorbed gas quantity, v_m is the monolayer adsorbed gas quantity and c is the BET constant.

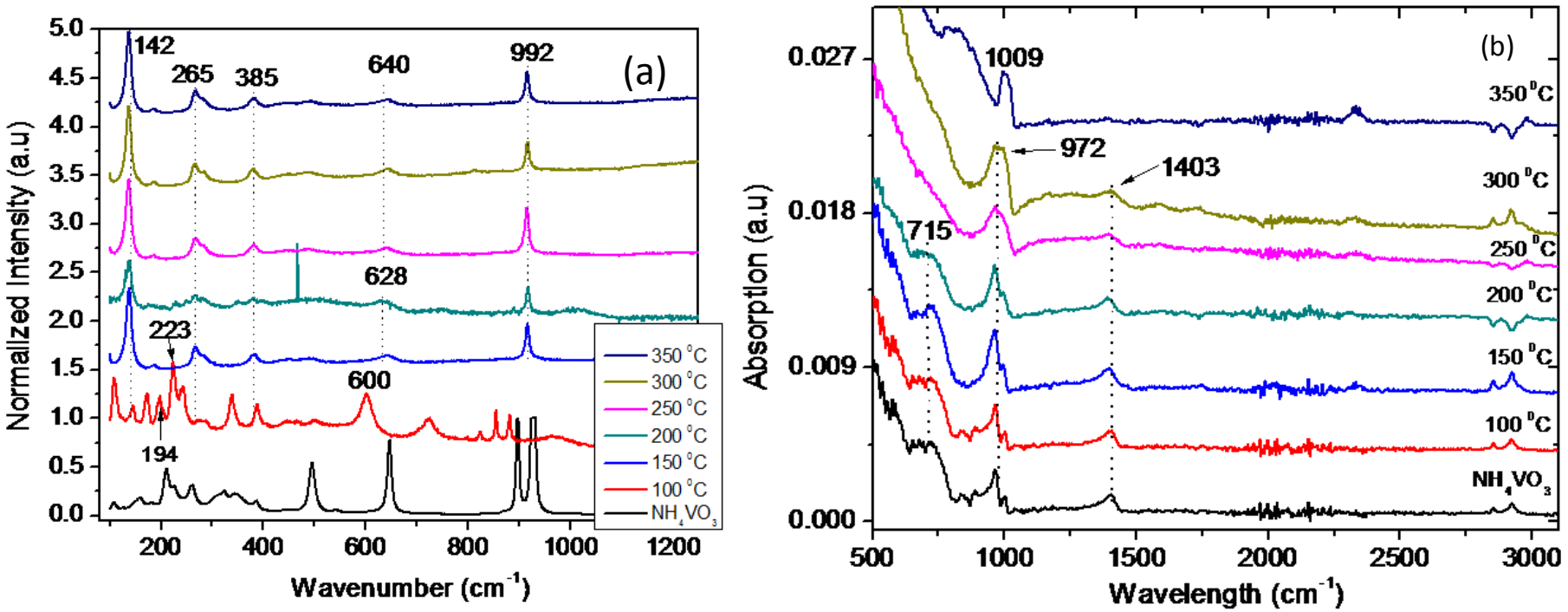

Figure 5: (a): Raman spectra of the standard NH_4VO_3 and of the samples prepared by calcination of NH_4VO_3 from 100 to 350 °C (b): FT-IR of the standard NH_4VO_3 and of the samples prepared by calcination of NH_4VO_3 from 100 to 350 °C.

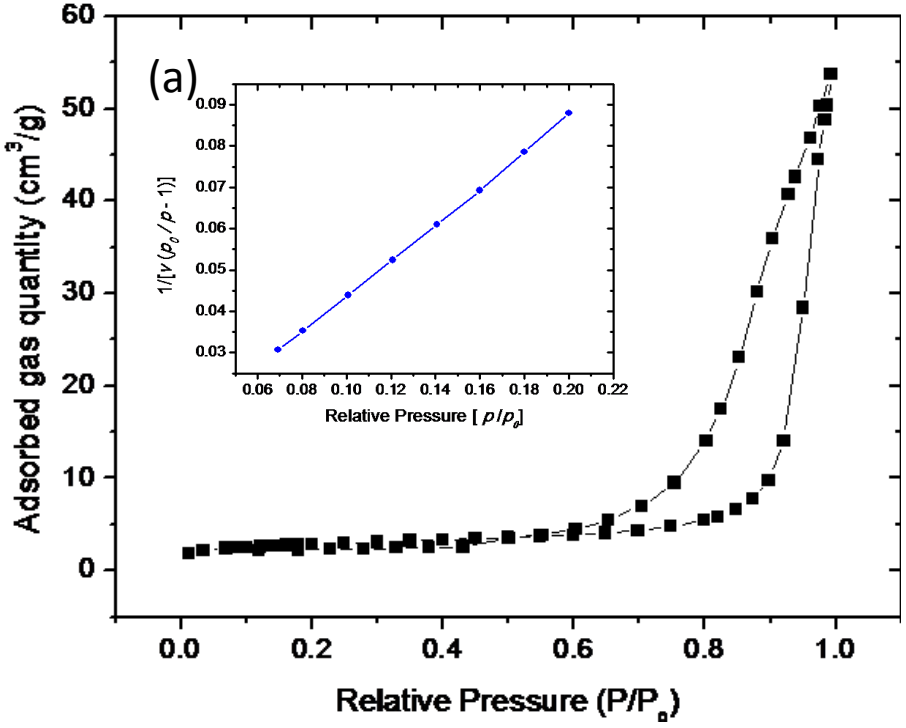

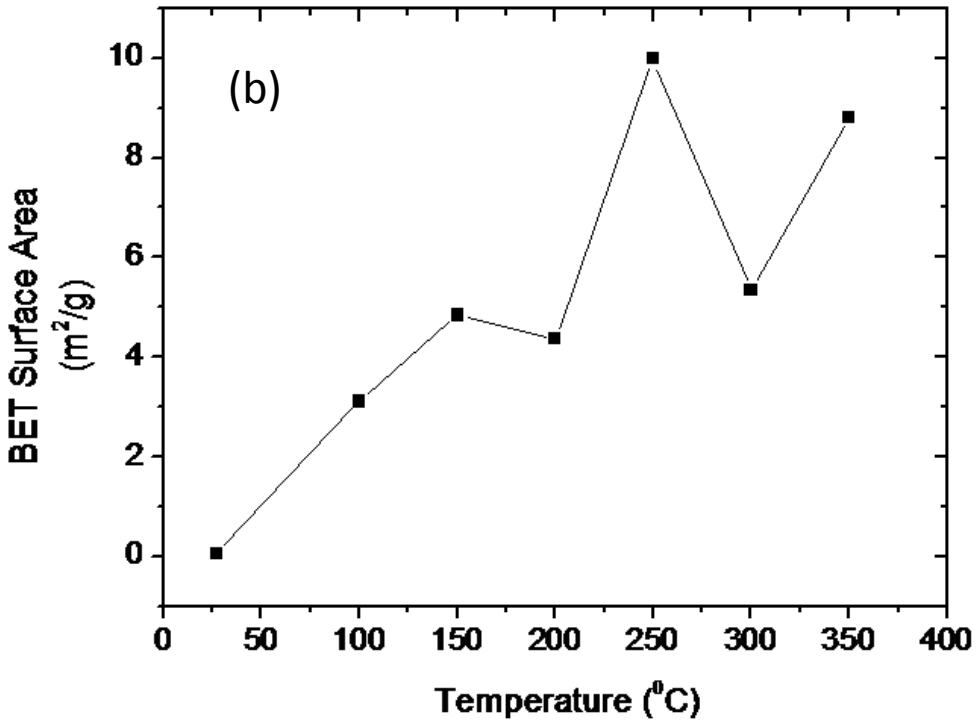

Figure 6: (a): N2 adsorption and desorption isotherms profile of the powder calcined at 250 °C, insert is the BET plot, (b): BET surface area versus temperature for all the calcined powders and including NH_4VO_3.

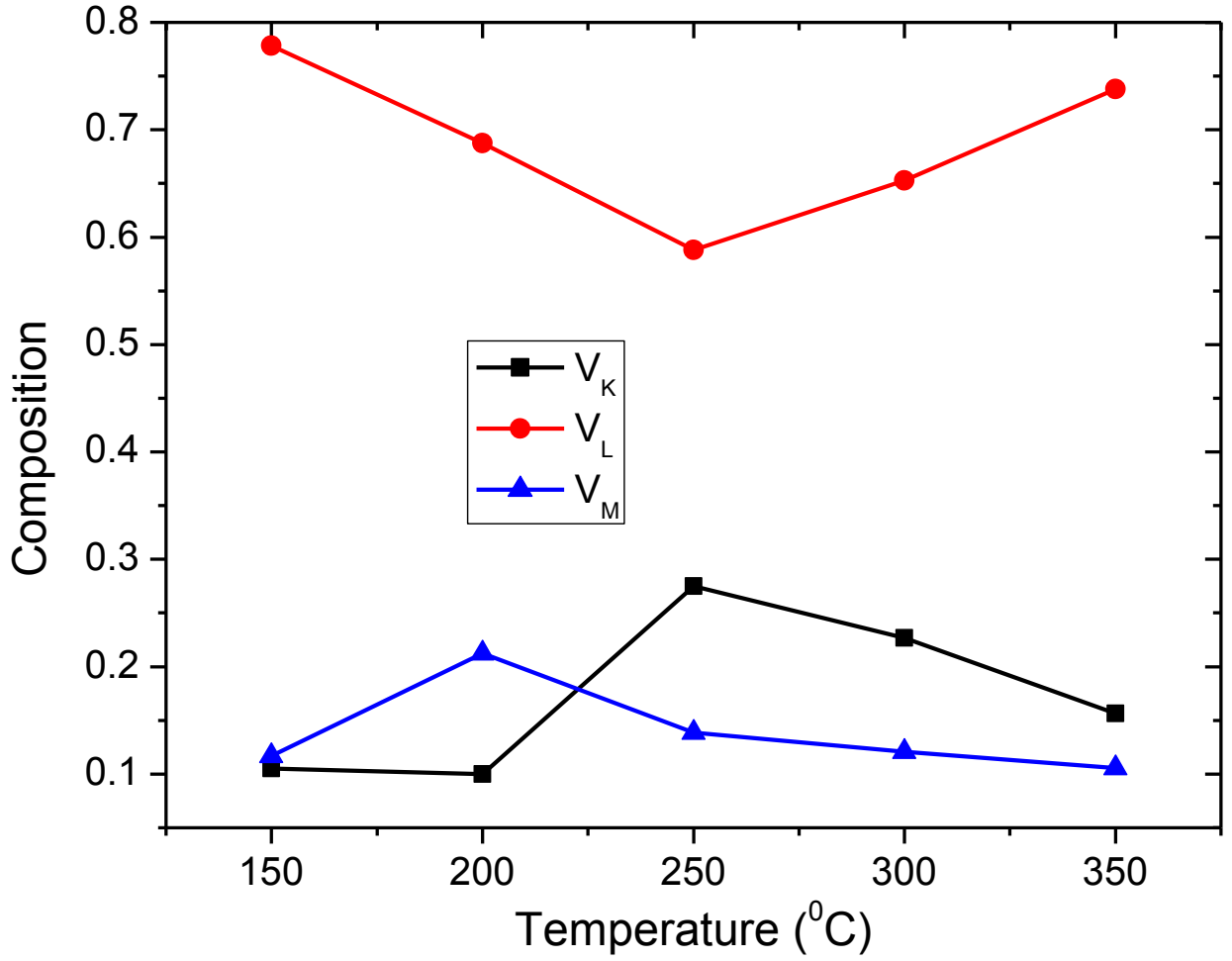

Figure 7: Proportions of V2O5, VO2 and V6O13 determined by EDS calibrated with XPS as they vary with annealing temperature.

The BET measurements were carried out for standard and calcined NH_4VO_3 at various temperatures 100 to 350^0C. The change in N_2 adsorption with partial pressure for the sample calcined at 250 ^{0}C is shown in figure 6(a). The monolayer adsorbed gas v_m and BET constant c were measure as the intercept of linear plot of $1/v(p_0/p - 1)$ and $p/p_{0,}$ shown in inset image fig. 6(a). The BET surface area ($S_{BET} = v_m.N_s/Va$, where Ns is Avogadros number, V is molar volume of adsorbate gas and a is the mass of the adsorbent) of calcined samples were calculated and are shown in fig. 6 (b). The surface area is found to increase with the calcination temperatures. It follows the Langmuir isotherms pattern with temperatures.

3.8 XPS and EDS

We have performed XPS on a reference sample containing known mixed V^{3+}, V^{4+} and V^{5+} phases of VO_x as well EDS of the same reference sample. The full XPS and EDS spectra this reference sample was reported in our recent paper [48]. This analysis has been used to calibrate all EDS results for the our current samples containing V_6O_{13}, VO_2 and V_2O_5. The analysis results are summarized in Table 1. First the heights and the widths of the peaks were determined for each peak in XPS and in EDS and areas under such peaks were calculated. The proportions were determined from the ratio of the area under each peak to the total of all peaks considered [47].

From Table 1 (a) the reference sample has 69% proportion of V_2O_5 or a contribution from mixed (metastable) V_6O_{13} and the rest 31% of the photo-electrons come from VO_2 with a small contribution from V_6O_{13} again. EDS results of the same sample indicate 70% X-ray emission from V_L electronic shell. This could be attributed to V_2O_5 and a small contribution from the mixed phase V_6O_{13} as suggested by XPS in Table 1 (a). EDS This shows that XPS

Table 1 (a): XPS analysis for reference or standard sample containing VO2, V2O5, V6O13 and WO3.

Orbitals	Height, H (a.u)	H0 (a.u.)	Width, W (eV)	A	% V + W	% of V^{i+}
$W(4f)_{7/2}$, W^{6+}	2100	150	3	5850	51.5	
$W(4f)_{5/2}$, W^{6+}	1600	250	3	4050	35.6	
$V(2p)_{3/2}$, V^{4+}	3500	3200	1.5	450	3.9	30.8
$V(2p)_{3/2}$, V^{5+}	3975	3300	1.5	1012.5	8.9	69.2

Table 1 (b): EDS analysis for reference or standard sample containing VO2, V2O5, V6O13 and WO3.

Electronic shell	Height, H (a.u)	Width, W (eV)	A	% of V^{i+}
V_M	500	0.2	100	15.6
V_L	1500	0.3	450	70.3
V_K	300	0.3	90	14.1

and EDS results are in good agreement and one can use local EDS results with this XPS calibration to determine the local composition of the current VO_x materials.

One can conclude the the V_L shell peak in EDS can be used to mark V_2O_5 whereas the V_M and V_K shells are mostly for VO_2 although in both cases V_6O_{13} has a strong indeterminate influence. One can understand the V_6O_{13} poses a challenge in ascertaining its exact contribution owing to its meta-stable nature.

We have summarized the EDS analysis results from the VOx samples annealed at 150, 200, 250, 300 and 350 °C based on the calibration undertaken in Tables 1 (a) and 1(b). These results are summarized in Table 2. It can be observed that the proportions of the phases change with annealing temperature. The changes are plotted in Figure 7. The V_L – temperature profile shows a decrease from 100 °C to 250 °C and then increases again up to the annealing temperature of 350 °C. This profile agrees very well with the phase diagram shown in Figure 4 in the previous section. Similarly, the proportions determined from V_M peak at 150 °C which is exactly the VO_2 profile in the phase diagram in Figure 4 whereas the proportions calculated from V_K shell increase to a maximum value at an annealing temperature of 200 °C which agrees with the V_6O_{13} profile in Figure 4. This assures us that the present XPS calibration of the EDS results is correct.

3.9 Vibrating Sample Magnetometry (VSM)

The traditional definitions of remanent magnetization (M_R^+ and M_R^-), saturation magnetization (M_S^+ and M_S^-) and squareness (SQ) in bulk and nano-scale magnetic materials are schematically illustrated in Figure 8 (a and b). It should be noted that nano-materials display a shift of the hysteresis loop due to what is called exchange bias [48,49]. In Figure 8

Table 2: EDS analysis based on the calibrations in Tables 1 (a) and (b) and local composition for the VOx samples annealed at 150, 200, 250, 300 and 350 C

Sample	Electronic shell	Height, H (a.u)	Width, W (eV)	A	% of Vi+
EDX 150	V_M	900	0.15	135	10.5
	V_L	5000	0.2	1000	77.8
	V_K	750	0.2	150	11.7
EDX 200	V_M	800	0.1	80	10.0
	V_L	5500	0.1	550	68.8
	V_K	850	0.2	170	21.2
EDX 250	V_M	530	0.15	79.5	27.5
	V_L	1700	0.1	170	58.7
	V_K	200	0.2	40	13.8
EDX 300	V_M	250	0.15	37.5	22.7
	V_L	720	0.15	108	65.2
	V_K	100	0.2	20	12.1
EDX 350	V_M	990	0.15	148.5	15.7
	V_L	3500	0.2	700	73.8
	V_K	500	0.2	100	10.5

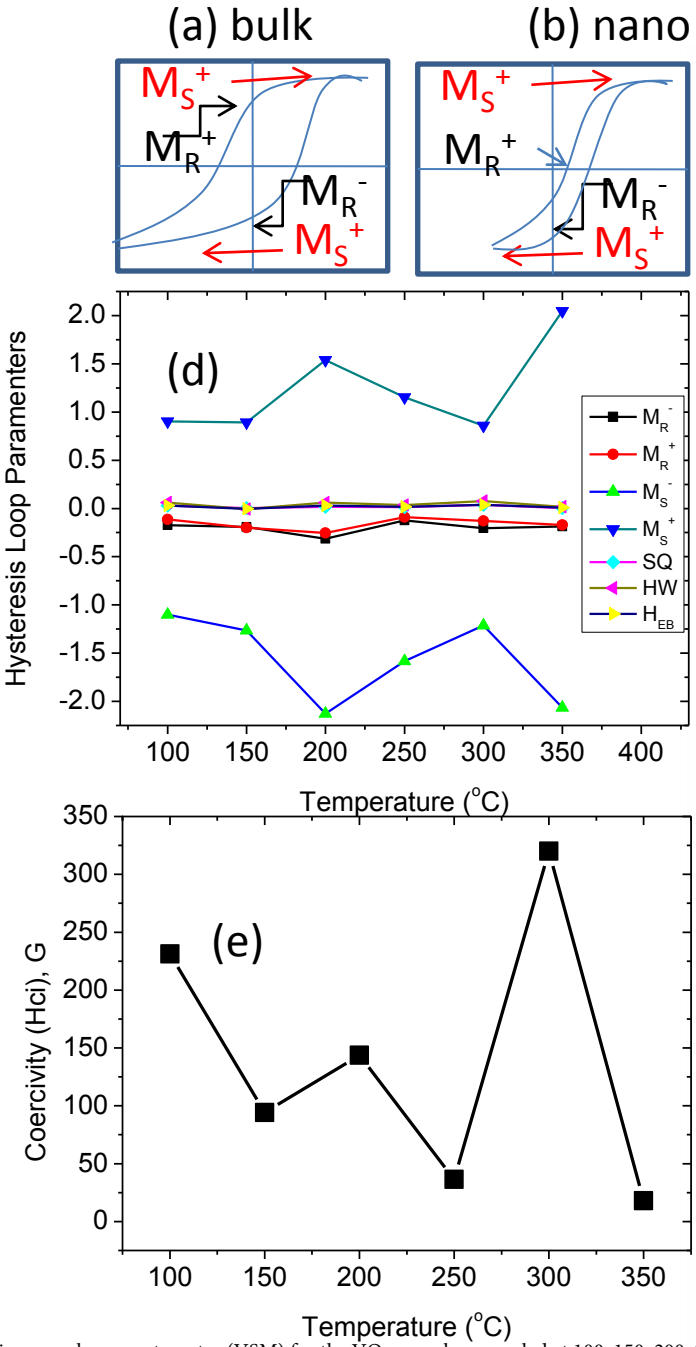

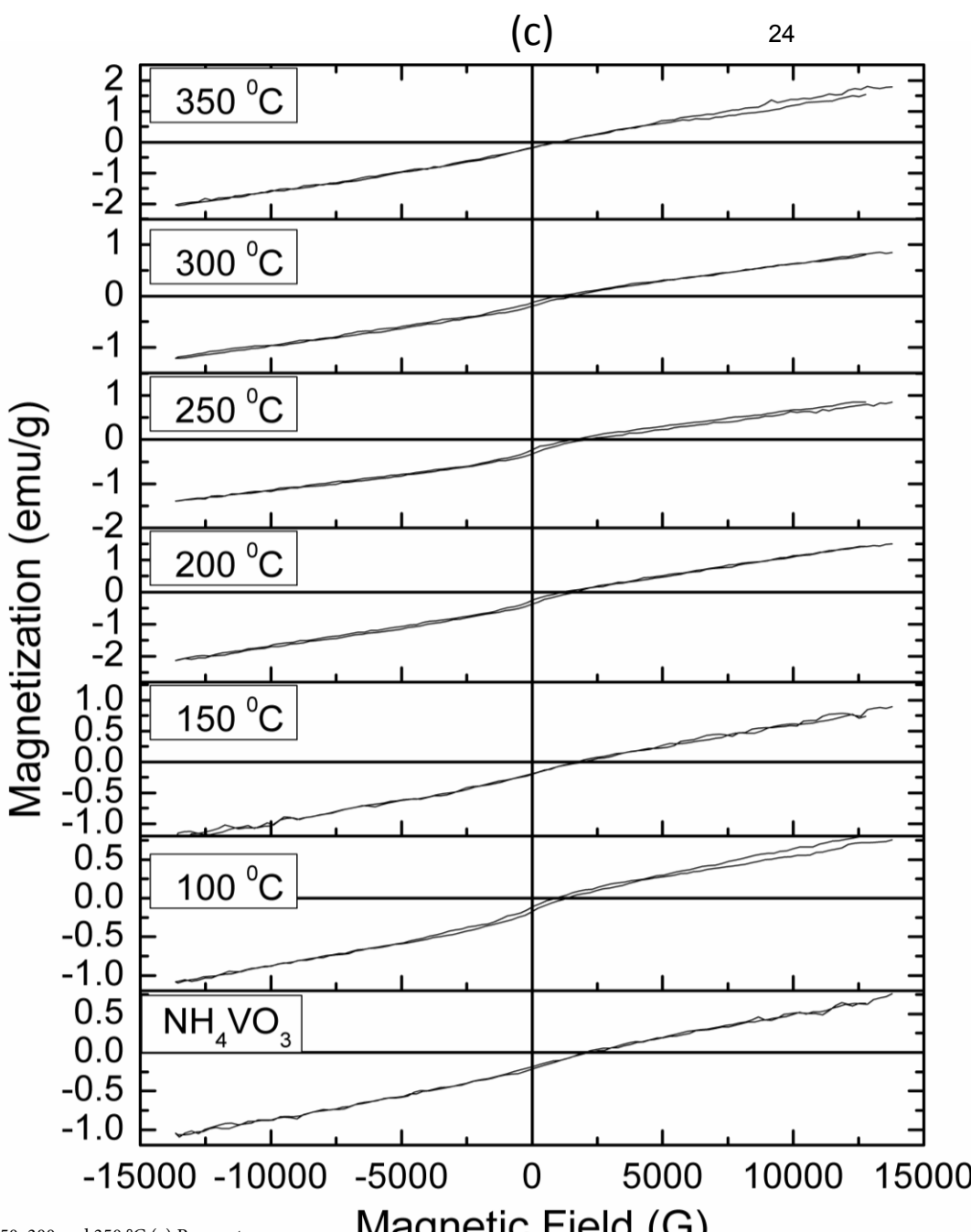

Figure 8: Vibrating sample magnetometry (VSM) for the VOx samples annealed at 100, 150, 200, 250, 300 and 350 °C (a) Parameters definition for a hysteresis loop for bulk and nano materials (b) Hystersis loops for VOx samples annealed at 100, 150, 200, 250, 300 and 350 °C and (c) A plot of the hysteresis loop parameters against annealing

(c) we show that hysteresis loops for all VO_x samples annealed at 100, 150, 200, 250, 300 and 350 °C including the precursor materials of ammonium metavanadate, NH_4VO_3. One can note that all samples show a degree of shift in the hysteresis loops which reveals that all the powders are nano-scale materials. As to whether these materials are ferro- or ferri- or para-magnetic, the loops show very small amount of squareness, of the order of 10^{-2}, and a very small opening in the loops [typical values of H_c^+-H_c^- of the order of 10^{-2}]. This points to the fact that these materials are largely para-magnetic. However, there is a finite coercivity (Figure 8 d and e) in samples (from 17 to 300 G) showing there is a degree of ferro-magnetic order in this paramagnetic matrix.

In Table 3 we give a summary of the parameters of remanent magnetization (M_R^+ and M_R^-), saturation magnetization (M_S^+ and M_S^-) and squareness (SQ) as well hysteresis width and exchange bias width obtained from the hysteresis loops given in Figure 8 (b). The hysteresis width has been estimated to be proportional to the loop opening in the vertical axis which is the difference between M_R^+ and M_R^-.

$$HW \propto \left(M_R^+ - M_R^-\right) = k\left(M_R^-(high) - M_R^-(low)\right) \quad (9)$$

The exchange bias width has been estimated to be half of this opening as previous done [50].

$$H_{EB} \propto \frac{\left(M_R^+ - M_R^-\right)}{2} = \frac{k}{2}\left(M_R^-(high) - M_R^-(low)\right) \quad (10)$$

A plot of these parameters for all annealed samples is given in Figure 8 (d,e) and it is interesting to note that coercivity generally decreases with annealing temperature although it shows a high point at 300 °C whereas remanent magnetization (M_R^+ and M_R^-), saturation magnetization (M_S^+ and M_S^-) all show the lowest values at 200 °C. At the former temperature, it is interesting to note that this is a transition temperature from V_6O_{13} to V_2O_5

Table 3 A summary of the hysteresis loop parameters of remanent magnetization (MR+ and MR-), saturation magnetization (MS+ and MS-) and squareness (SQ) as well hysteresis width and exchange bias width

Annealing Temp oC	Coercivity (Hci), G	MR Negative, emu/g	MR Positive, emu/g	MS Negative, emu/g	MS Positive, emu/g	Squareness	Loop opening emu/g	Exchange bias emu/g
100	231.12	-0.17	-0.11	-1.10	0.90	0.03	0.06	0.03
150	94.32	-0.19	-0.20	-1.26	0.89	0.00	-0.01	0.00
200	143.64	-0.31	-0.25	-2.13	1.54	0.02	0.06	0.03
250	36.42	-0.12	-0.09	-1.58	1.15	0.01	0.04	0.02
300	320.09	-0.20	-0.13	-1.21	0.86	0.04	0.08	0.04
350	17.90	-0.19	-0.17	-2.06	2.05	0.00	0.02	0.01

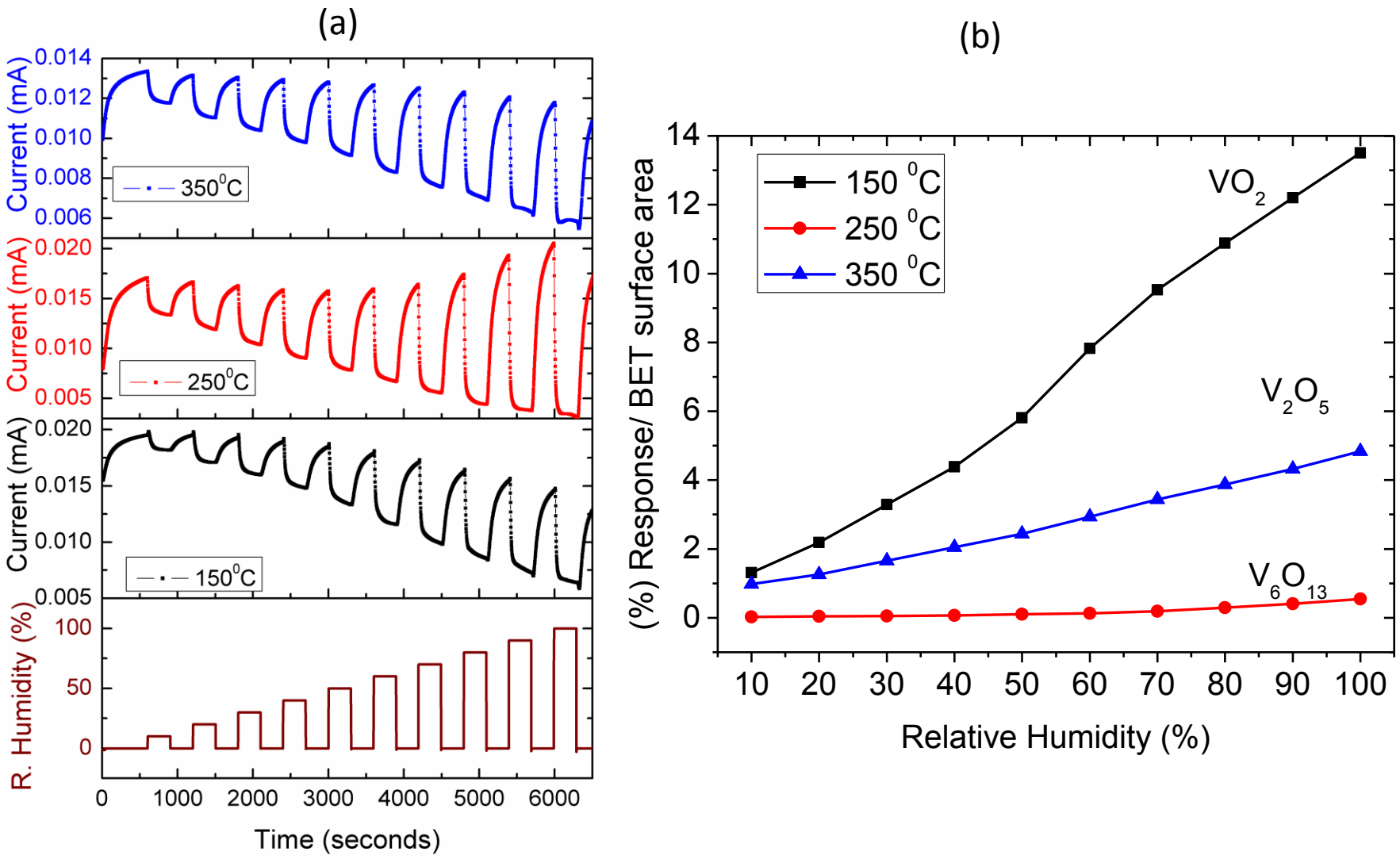

Figure 9: (a) Transient profiles of current through the VOx samples in varying levels of humidity (b) Responses weighted against BET surface area for VOx samples as function of humidity level.

and the latter is a transition temperature from VO_2 to V_6O_{13}. VSM confirms the following order of appearance: $VO_2 \rightarrow V_6O_{13} \rightarrow V_2O_5$ as temperatures of annealing are elevated.

3.10 Applications: Humidity Sensing.

We have shown before how VO_2 has been employed in sensing of hydrogen [51,52]. In this present report, we have also subjected the VO_x samples annealed at 150 °C (VO_2), 250 °C (V_6O_{13}) and 350 °C to sensing of humidity. The transient profiles of the current through the sample placed on inter-digitated electrodes in the presence or absence of varying humidity levels are shown in Figure 9 (a). Each time the humidity level is allowed in the chamber, the current through the samples decreases. This means that all VOx samples gain resistance upon interaction with water vapour. Since all these VOx phases are known to show n-type conductivity, we could explain the increase in resistance as an indication of water molecules taking away electrons or O2- species from VOx surfaces during adsorption but releasing these electrons back on desorption. In Figure 9 (b) we plot response [defined as $S = (I_{out}-I_{in})/I_{in}$] as a function of humidity level. This plot reveals the Langmuir type of adsorption-desorption isotherms.

4. **Conclusion**

A few milligrams of ammonium metavanadate powders were calcined in pure hydrogen atmosphere at temperature of 100, 150, 200, 250, 300 and 350 °C. The samples were characterized by TGA/DSC, XRD, TEM, Raman spectroscopy, FTIR,BET, VSM and XPS/EDS. All these characterization methods lead us to conclude that the progression from NH_4VO_3 to V_2O_5 is as follows: $NH_4VO_3 \rightarrow VO_2+V_2O_5$ (150-200°C)$\rightarrow V_6O_{13}$ (300°C) $\rightarrow V_2O_5$ (above 325°C). At no temperature does one find a single phase; each temperature of calcinations will have a major and a minor phase or a number minor phases. The total surface

area appears to increase with a decreasing rate as the temperature of calcinations is increased. A phase diagram based on XRD and Raman has been constructed for VO_2, V_6O_{13} and V_2O_5. XPS/EDS analysis agrees with this phase diagram. It is also found that VSM confirms the order of $VO_2 \rightarrow V_6O_{13} \rightarrow V_2O_5$ transitions as temperatures of annealing are elevated.

5. **Acknowledgements**

Support from the India-Brazil-South Africa trilateral cooperation under the National Research Foundation (NRF) grant number HGER24X is acknowledged.

References

[1] P. S. Matsumoto, Trends in Ionization Energy of Transition-Metal Elements, J. Chem. Education, Vol. 82, No. 11, 2005.

[2] X. Chen, X. Wang, Z. Wang, J. Wan, J. Liu, Y. Qian, An ethylene glycol reduction approach to metastable VO_2 nanowire arrays, Nanotech. 15 (2004) 1685-1687.

[3] M. Imada, A. Fujimori, Y. Tokura, Metal-insulator transitions, Rev. of Modern Phy. 70, No.4 1039-1263 (1998).

[4] N.F. Mott, Metal-insulator Transition, Rev. Modern Phys. 40 (4) (1968) 677.

[5] D. Adler, Mechanisms for Metal-Nonmetal Transitions in Transitions-Metal Oxides and Surfides, Rev. Modern Phys. 40 (4) (1968) 714-736.

[6] F.J. Morin, Oxides which show a metal-insulator-transition at Neel temperature, Phys. Rev. Lett. 3, (1959) 34.

[7] J.B. Goodenough, The two components of Crystallographic transition in VO_2, J. Solid State Chem. 3, 490-500 (1971).

[8] S. Shin, S. Suga, M. Tanuguchi, M. Fijisawa, H. Kansaki, A. Fujimori, H. Damon, Y. Ueda, K. Kosuge, S. Kachi, Vacuum-ultraviolet reflectance and photoemission study of the metal - insulator phase transitions in VO_2, V_6O_{13}, and V_2O_3, Phys. Rev. B 41, 4993-5009 (1990).

[9] J.M. Reyes, J.R. Marko, M. Sayer, Hysteresis in the Semiconductor-Metal Transition of Cr-doped VO_2, Solid State Comm., Vol. 13 1953-1957 (1973).

[10] D. Paquet, P. Leroux-Hugon, Electron correlations and electron-lattice interactions in themetal-insulator, ferroelastic transition in VO_2: A thermodynamical study, Phys. Rev. B22, 5284-5301 (1980).

[11] N.F. Mott, R. Peierls, Discussion of the paper by de Boer and Verwey Proc. Phys. Soc. London, Ser. A. 49, 72 (1937).

[12] A. I. Buzdin, L N. Bulaevskii, P. N. Lebedev, Spin-Peierls transition in quasi-one dimensional crystals**,** Physics Institute, Academy of Sciences of the USSR, Moscow Usp Fiz Nauk, 131, 495-510 (July 1980).

[13] G.I. Petrov, V.V. Yakovlev, Raman microscopy analysis of phase transformation mechanisms in vanadium dioxide, App. Phy. Lett. Vol. 81. No. 6 (2002).

[14] S.-Y. Li, G. A. Niklasson, and C. G. Granqvist, Nanothermochromics: Calculations for VO_2 nanoparticles in dielectric hosts show much improved luminous transmittance and solar energy transmittance modulation, J. Appl. Phys. 108, 063525 (2010).

[15] R. Lopez, R. F. Haglund, Jr., L. C. Feldman, L. A. Boatner, T. E. Hayness, Optical nonlinearities in VO_2 nanoparticles and thin films, App. Phy. Lett 85, (2004).

[16] S. Lysenko, A. Rua, F. Fernandez, H. Liu, Vanadium dioxide based plasmonic modulators, J. Appl. Phys. 105, 043502 (2009)

[17] J. Cao, W. Fan, J-Q. Wu, Strain and temperature dependence of the insulating phases of VO_2 near the metal-insulator transition, Phy. Rev. B 85, 020101(R) (2012)

[18] Z. Lu, C-G.Lia,Y. Yin, Synthesis and thermochromic properties of vanadium dioxide colloidal Particles, J. Mater. Chem., 2011, 21, 14776-14782

[19] E .U. Donev, J. I. Ziegler, R. F Haglund Jr., L. C. Feldman, Size effects in the structural phase transition of VO_2 nanoparticles studied by surface-enhanced Raman scattering, J. Opt. A: Pure Appl. Opt. 11(2009) 125002 (8pp).

[20] A. C. Jones, S. Berweger, J. Wei, D. Cobden, M. B. Raschke, Nano-optical investigations of the metal-insulator phase behaviour of individual VO_2 microcrystals, Nano Lett. 2010, 10, 1574–1581.

[21] M. Maaza, O. Nemraoui, C. Sella, A. C. Beye, B. Baruch-Barak, Thermal induced tenability of surface plasmon resonance in Au-VO_2 nano-photonics, Optics Comm. 254 (2005) 188-195.

[22] A. Pergrament, G. Stefanovich, O. Berezina, D. Kirienko, Electrical conductivity of tungsten doped vanadium dioxide obtained by the sol-gel technique, Thin Solid Films 572-576 (2013)

[23] Y. Gao, H. Luo, Z. Zhang, L. Kang, Z. Chen, J. Du, M. Kanehira, C. Cao, Nanoceramic VO_2 thermochromic smart glass: A review on progress in solution processing, Nano Energy (2012) 1, 221-246.

[24] W. Burkhardt, T. Christmann, B.K. Meyer, W. Niessner, D. Schalch, A. Scharmann , Wand F-doped VO_2 films studied by photoelectron spectrometry, Thin Sol. Films. 345 (1999) 229-235.

[25] O. Y. Berezina, A. A. Velichko, L.A. Lugovskaya, A.L. Pergament, G.B. Stefanovich, D.V. Artyukhin, A. N. Strelko, Properties of Tungsten-Doped Vanadium Oxide Films, Tech. Phys. Lett. (2007) Vol. 33, No. 7, pp. 552-555.

[26] R. Binions, G. Hyett, C. Piccirillo, I. P. Parkin, Doped and Undoped vanadium dioxide thin films prepared by atmospheric pressure chemical vapour deposition from vanadyl

acetylacetonate and tungsten hexachloride: the effects of thickness and crystallographic orientation on thermocromic properties, J. Mat. Chem. 17, 4652-4660 (2007)

[27] E. Strelcov, Y. Lilach, A. Kolmakov, Gas Sensor Based on Metal-Insulator Transition in VO_2 Nanowire Thermistor, Nano Letters 2009, Vol. 9, No. 6, 2322-23269

[28] C.G. Granqvist, Electrochromic tungsten oxide films: Review of progress 1993- 1998, Solar Energy Materials & Solar Cells 60 (2000) 201- 262

[29] J. Livage_, D. Ganguli, Sol-gel electrochromic coatings and devices: A review, Solar Energy Materials & Solar Cells 68 (2001) 365-381

[30] J. Huotari, A. L. Spetz1, J. Lappalainen, Gas Sensing Properties of Pulsed Laser Deposited Vanadium Oxide Thin Films, The 14th International Meeting on Chemical Sensors, IMCS 2012.

[31] M.C. Rao, Vanadium Pentoxide Cathode Material for Fabrication of All Solid State Lithium-Ion Batteries - A Case Study, Res. J. Recent Sci. Vol. 2(3), 67-73, March (2013)

[32] P. Kiria, G. Hyettb, R. Binions , Solid state thermochromic materials, Adv. Mat. Lett. 2010, 1(2), 86-105.

[33] H. Bai, M. Berkahn, M.B. Cortie, 31 Annual Condensed Matter and Materials 2007

[34] L. Chen, Ch. Huang, G. Xu, L. Miao, J. Shi, J. Zhou, X. Xiao, Synthesis of Thermochromic W-Doped VO_2 (M/R) Nanopowders by a Simple Solution-Based Process**,** J. Nanomaterials, (2012) 1-8, doi:10.1155/2012/491051

[35] M. Taniguchi, T.R. Ingraham, Mechanism of thermal decomposition of Ammonium metavadate, Canadian Journal of Chemistry, (1964) 42(11) 2467-2473

[36] B.W. Mwakikunga, E. Sidras-Haddad, M. Maaza, First synthesis of vanadium dioxide by ultrasonic nebula-spray pyrolysis, Optical Materials 29 (2007) 481-487

[37] B.W. Mwakikunga, M. Maaza, K.T. Hillie, C.J. Arendse, T. Malwela, E. Sideras-Haddad, From phonon confinement to phonon splitting in flat single nanostructures: A case of VO_2@V_2O_5 core–shell nano-ribbons, Vibrational Spectroscopy 2025 (2012).

[38] X. Wua, Y. Taoa, L. Donga, Z. Wangb, Z. Hua, Preparation of VO_2 nanowire and their characterization, Mat. Res. Bullet. 40 (2005) 315–321

[39] U.V. Sacken, J.R. Dahn, TGA/MS Studies of the thermal decomposition of NH_4VO_3, J. Power Sources, 26 (1989) 461-465

[40] M.E. Brown, B.V. Stewart, The thermal decomposition of ammonium metavanadate, J. Thermal Anal. Vol. 2 (1970) 287-299

[41] J. Twu, C-F. Shih, T-H, Guo, K-H, Chen, Raman spectroscopic studies of the thermal decomposition mechanism of ammonium metavanadate, J. Mater. Chem., 1997 7 (11) 2273-2277

[42] C. Julien, G. A. Nazri, and O. Bergstrom, Raman Scattering Studies of Microcrystalline V6O13, Phys. Stat. Solidi B 201, 319-326 (1997)

[43] D. Vernardou, M. Apostolopoulou, D. Louloudakis, E. Spanakis, N. Katsarakis, E. Koudoumas, J. MacGrath, M.E Pemble, Electrochemical properties of Opal-V_6O_{13} composites, J. Alloy and Compound 2014 (582) 621-626.

[44] K. Virkler, I. K. Lednev, Raman spectroscopic signature of semen and its potential application to forensic body fluid identification, Forensic Science International 193 (2009) 56–62

[45] I.L. Botto, M.B. Vassallo, E.J. Baran, G. Minelli, IR spectra of VO_2 and V_2O_5, Matt. Chem. and Phy. 50 (1997) 267-270.

[46] S. Brunauer , P. H. Emmett , E. Teller, Adsorption of Gases in Multimolecular Layers, *J.* Am. Chem. Soc., 1938, 60 (2), pp 309–319

[47] R. F. Karlak, D. S. Burnett, Quantitative phase analysis by X-ray diffraction, Analytical Chem. 38 (1966) 1741-1745

[48] A.A. Akande , K. E. Rammutla, T. Moyo, N. S.E. Osman, Steven S. Nkosi, C.J. Jafta, Bonex W. Mwakikunga, Magnetism variations and susceptibility hysteresis at the metal-insulator phase transition temperature of VO_2 in a composite film containing vanadium and tungsten oxides, J Magn. Magn. Mater. 375 (2015) 1–9

[49]] J. Nogués, J. Sort, V. Langlais, V. Skumryev, S. Surinack, J.S. Munoz, M.D. Baró, Exchange bias in nanostructures, Phys. Rep. 422 (2005) 65–117

[50] K. Mbela, T. Moyo, J.Z. Msomi, M. Ozturk, N. Akdogan, Synthesis and magnetic properties of $Mg_{0.2}Cr_{1.8-x}Fe_xO_3$, J. Magn. Magn. Mater. 330 (2013) 159-162

[51] B. W. Mwakikunga, S. Motshekga, L. Sikhwivhilu, Mathew Moodley, M. Scriba, Gerald Malgas, A. Simo, B. Sone, M. Maaza, Suprakas Sinha Ray, A classification and ranking system on the H2 gas sensing capabilities of nanomaterials based on proposed coefficients of sensor performance and sensor efficiency equations, Sensors & Actuators B 184 (2013) 170–178

[52] A. Simo, B. Mwakikunga, B. T. Sone, B. Julies, R. Madjoe, M. Maaza, VO2 nanostructures based chemiresistors for low power energy consumption hydrogen sensing, Int. J. of Hydrogen Energy 39 (2014) 8147 - 8157

Highlights

- Validated the theoretical mass losses at each temperature of NH_4VO_3 with TGA
- Confirmed mechanisms of formation of various stoichiometries of VO_x from NH_4VO_3
- Determined the evolution of VO_2, V_6O_{13} and V_2O_5 with temperature.
- Phase diagram of VO_2, V_6O_{13} and V_2O_5 by VSM, XPS/EDS, XRD and Raman spectra
- Comparative response of VO_2, V_6O_{13} and V_2O_5 to humidity

APPENDIX A SUPPLEMENTARY DATA

SM1

A 4.726 mg of NH_4VO_3 powder was introduced into TGA system, the molar mass of NH_4VO_3 is 116.98g and the number of mole based on the weight of NH_4VO_3 is calculated as 4.04 x 10^{-5} mol. The decomposition mechanisms (1 – 5) in the full manuscripts were considered with mechanism (3) found to be an applicable mechanism in our case.

$$4NH_4VO_3 \rightarrow (NH_4)_2V_4O_{11} + 2NH_3(g) + H_2O(g) \quad (3)$$

Molar mass of other components $(NH4)_2V_4O_{11}$, NH_3 and H_2O were estimated as 415.834g, 17.0307g and 18.0148g respectively.

The following calculations were performed as follows,

Mass of $(NH4)_2V_4O_{11}$ = (4.04 x 10^{-5}/4) x 415.834 = 4.199 x 10-^{3}g

Mass of NH_3 = (4.04 x 10^{-5}/2) x 17.0307 = 3.44 x 10^{-4} g

Mass of H_2O = (4.04 x 10^{-5}/4) x 18.0148 = 1.819 x 10^{-4}g

Total mass of all components in this mechanism is found to be 4.7249 x 10^{-3} g which validates mechanism 3 as the process involved in our experiment.

SM2

TGA residual mass of V_6O_{13} powder (fig. 1(c)) at 147.9 ^{0}C is recorded as 4.9702 mg and its molar mass is found to be 513.639g. The number of mole is calculated as expressed below.

Number of mole = 4.9702 x 10^{-3}/513.639 = 9.676 x 10^{-6} mol.

Mechanism (6) in the full manuscript was proposed.

$$2V_6O_{13} \rightarrow 12VO_2 + O_2 \quad (6)$$

Molar mass of other components VO_2 and O_2 were estimated as 82.94g and 31.998g respectively.

The following calculations were performed as follows,

Mass of VO_2 = 9.676 x 10^{-6} x 6 x 82.94 = 4.818 x 10^{-3}g

Mass of O_2 = 9.676 x 10^{-6} x 31.998 = 1.548 x 10^{-4}g

Total mass of all components is found to be 4.972 x 10^{-3}g which is also correspond to the mass at 147.9 ^{0}C.

The % mass loss (experimental) is calculated by subtracting the mass at 147.9^{0}C from the original mass introduce to the TGA system as express below.

% mass loss (experimental) = (5.093 – 4.9702) 10^{-3}/ 4.9702 x 10^{-3} x 100%

= 2.53%

The % mass loss (theoretical) is calculated by subtracting the mass of VO2 based on mechanism (6) from the total mass as expressed below.

% mass loss (theoretical) = (4.972 - 4.818) 10^{-3}/ 4.818 x 10^{-3} x 100%

= 3.09%

This show that the experimental value is close to theoretical, and that the conversion from V_6O_{13} to VO_2 is possible around 147.9^{0}C.

SM3

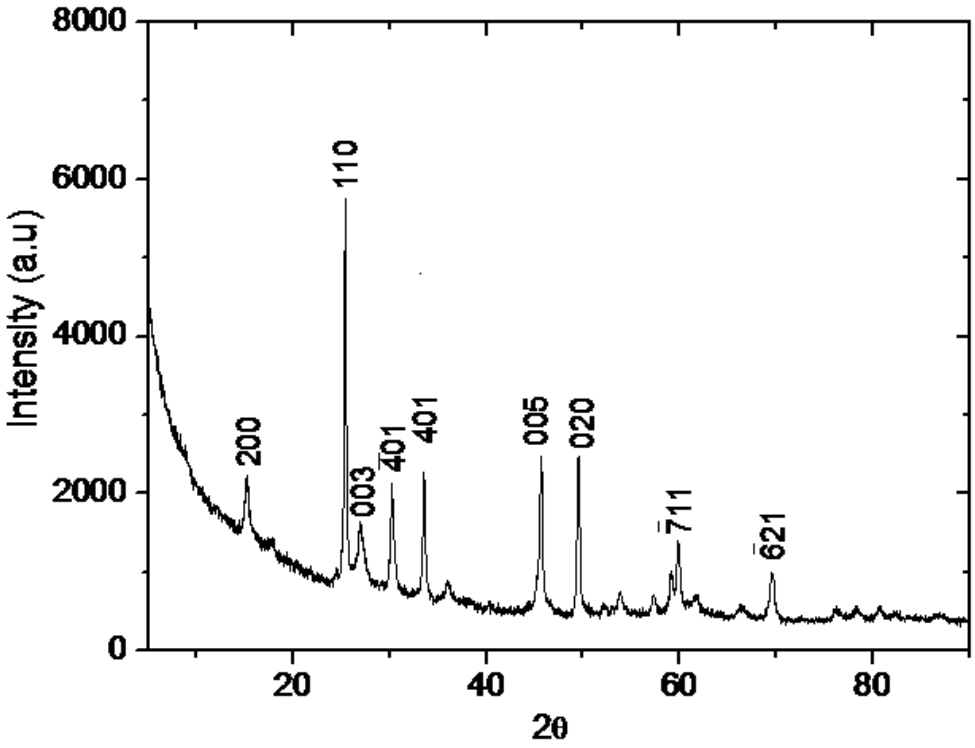

XRD pattern of the sample prepared at 400 ^{0}C

SM4

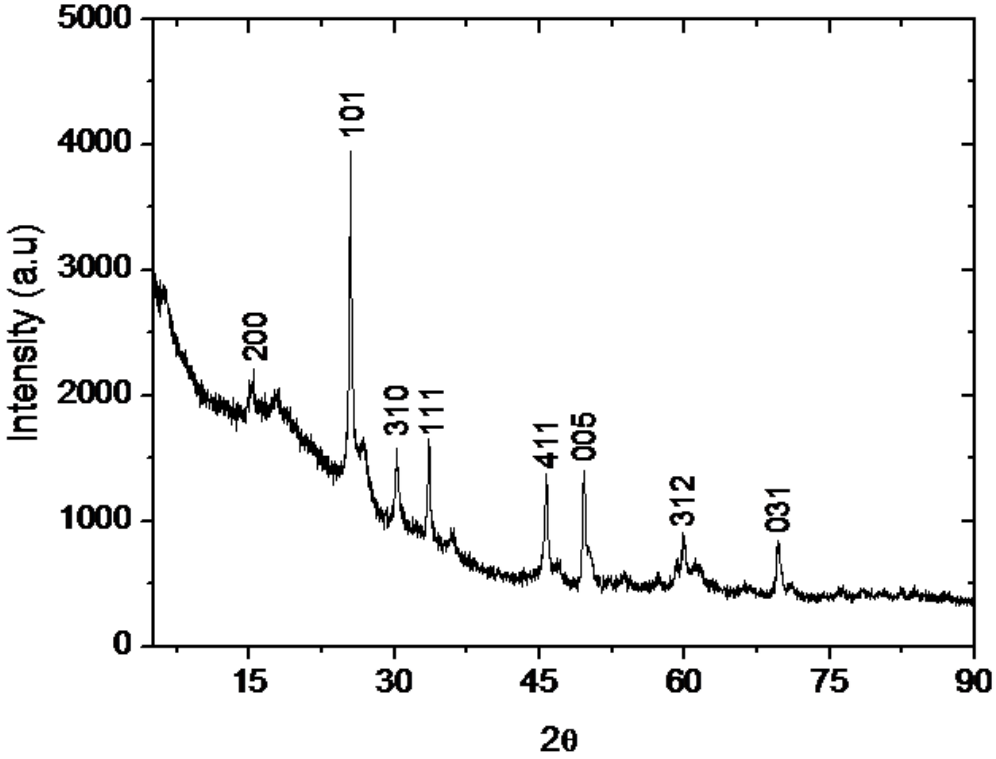

XRD pattern of the sample prepared at 500 ^{0}C

SM5

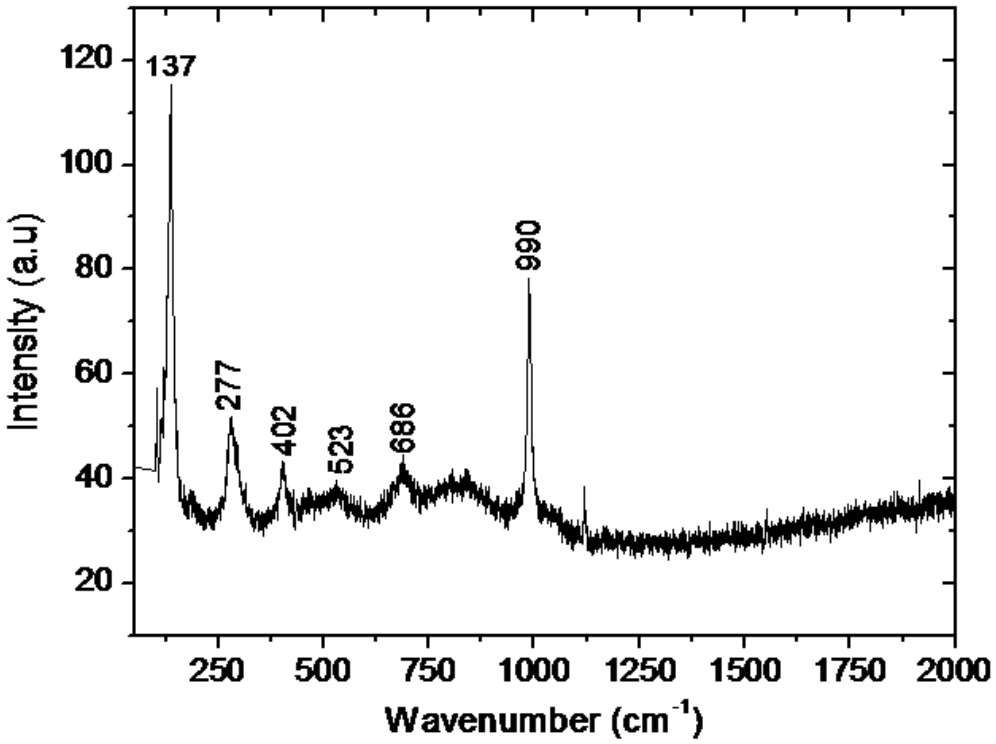

Raman spectrum of the sample prepared at 400 ^{0}C

SM6

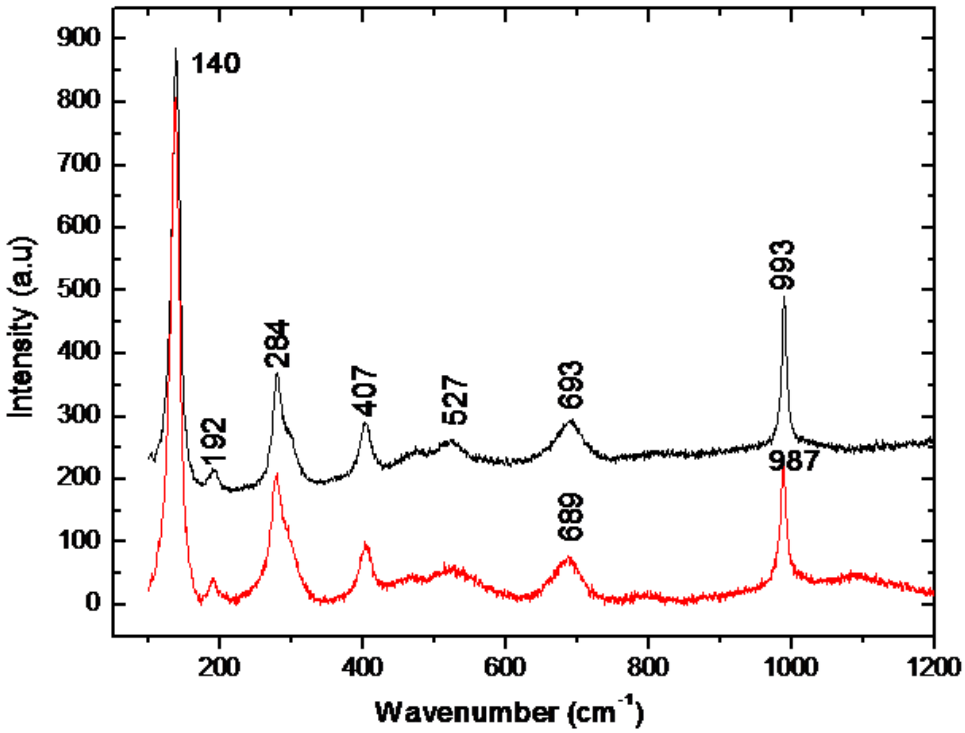

Black line is Raman spectrum of the sample prepared at 500 ^{0}C. Red line spectra is for NH_4VO_3 solution (V^{5+} state) drop cast on the corning glass substrates, similar vibration modes were achieved except 6 cm^{-1} blue shift at higher frequency modes of 993 and 987 cm^{-1}. This shows that NH_4VO_3 in the liquid state could be V_2O_5 in terms of its molecules vibration.